PHYSICAL REVIEW B **95**, 024308 (2017)

Phonons and elasticity of cementite through the Curie temperature

L. Mauger,[1] J. E. Herriman,[1] O. Hellman,[1] S. J. Tracy,[1] M. S. Lucas,[2] J. A. Muñoz,[1] Yuming Xiao,[3] J. Li,[4] and B. Fultz[1]
[1]*California Institute of Technology, W. M. Keck Laboratory 138-78, Pasadena, California 91125, USA*
[2]*Air Force Research Laboratory, Wright-Patterson AFB, Ohio 45433, USA*
[3]*HPCAT, Geophysical Laboratory, Carnegie Institute of Washington, Argonne, Illinois 60439, USA*
[4]*Department of Earth and Environmental Sciences, University of Michigan, Ann Arbor, Michigan 48109, USA*
(Received 22 December 2015; revised manuscript received 5 September 2016; published 20 January 2017)

Phonon partial densities of states (pDOS) of $^{57}Fe_3C$ were measured from cryogenic temperatures through the Curie transition at 460 K using nuclear resonant inelastic x-ray scattering. The cementite pDOS reveal that low-energy acoustic phonons shift to higher energies (stiffen) with temperature before the magnetic transition. This unexpected stiffening suggests strongly nonharmonic vibrational behavior that impacts the thermodynamics and elastic properties of cementite. Density functional theory calculations reproduced the anomalous stiffening observed experimentally in cementite by accounting for phonon-phonon interactions at finite temperatures. The calculations show that the low-energy acoustic phonon branches with polarizations along the [010] direction are largely responsible for the anomalous thermal stiffening. The effect was further localized to the motions of the Fe_{II} site within the orthorhombic structure, which participates disproportionately in the anomalous phonon stiffening.

DOI: 10.1103/PhysRevB.95.024308

I. INTRODUCTION

Cementite, Fe_3C, is the most common carbide in steels. Accordingly it has gathered much interest for its significant role in thermomechanical processing and how its presence in different microstructures affects material properties [1,2]. Cementite has also been considered as a candidate phase for the Earth's inner core, motivating a variety of studies at elevated pressures [3]. Despite the longstanding metallurgical interest in Fe_3C, many of its physical properties are still poorly constrained, because cementite is metastable at ambient conditions, requiring high pressures to synthesize the pure compound [4,5].

Cementite has an orthorhombic structure with the *Pnma* space group. The Fe atoms occupy the general 8*d* site (Fe_{II}) and the special 4*c* site (Fe_I). The carbon atoms also occupy the 4*c* site, with prismatically coordinated positions between the Fe atoms, as shown in Fig. 1. Both Fe sites have C atoms in the first-nearest-neighbor coordination shell, and a second-nearest-neighbor shell composed mostly of Fe-Fe bonds, with the closest Fe-Fe bond existing between Fe_{II} atoms along the *b* axis [7]. Cementite is ferromagnetically ordered at ambient pressures below 460 K, and at ambient temperatures below 7 GPa [8,9].

The temperature-dependent thermal expansion of Fe_3C, evaluated by neutron diffraction, exhibited unusual magnetovolume behavior, including regions of anomalously small and anisotropic thermal expansion in the ferromagnetic phase [10], High pressure studies of structure and magnetism showed that cementite exhibits magnetovolume anomalies similar to those of Invar alloys [11–15]. The temperature-dependent heat capacity of cementite remains poorly constrained by a wide range of experimental values reported on samples of varying origin and purity, and the high-temperature stability of Fe_3C is still controversial [10,16–20]. Without detailed experimental information for cementite, thermodynamic assessments of Fe_3C must rely on computational models [20]. However, quasiharmonic density functional theory calculations of Fe_3C are unable to reproduce the anomalous thermal expansion of the ferromagnetic phase [21].

The elastic properties of cementite are critical for understanding its role in strengthening steels, but comprehensive experimental studies are unavailable. First-principles studies indicate that ferromagnetic cementite has an unusually high elastic and shear anisotropy [19,22–24]. There are also computational predictions of strain stiffening in cementite under extreme deformations in specific crystal orientations [23]. The limited number of experimental studies of elastic behavior report that cementite does appear anisotropic, but not to the extent predicted by density functional theory [25,26]. An ultrasonic study of the elastic properties of Fe_3C reported anomalous thermal behavior at low temperatures [27]. The anisotropic elastic behavior of cementite is likely linked to its complex anisotropic magnetovolume behavior.

Here we report vibrational spectra of Fe_3C from cryogenic temperatures through its magnetic transition to help elucidate the underlying physics in this material. These measurements with supporting calculations provide the vibrational entropy of Fe_3C, and how it changes through the magnetic transition. We observe anomalous thermal stiffening of the low-energy phonons in ferromagnetic cementite. The anomalous vibrational trends are strongly correlated with the Fe_{II} sublattice and phonons polarized along the *b* axis. The elastic behavior was calculated and compared to the low-energy vibrational modes, and the elevated temperature phonon behavior provides information on the thermal trends in elastic moduli. The thermal trends of phonons and elastic constants undergo changes at the Curie temperature, suggestive of changes in magnon-phonon interactions.

II. METHODOLOGIES

A. Experiment

High pressure, high temperature synthesis was used to prepare $^{57}Fe_3C$ at stoichiometric composition. The material

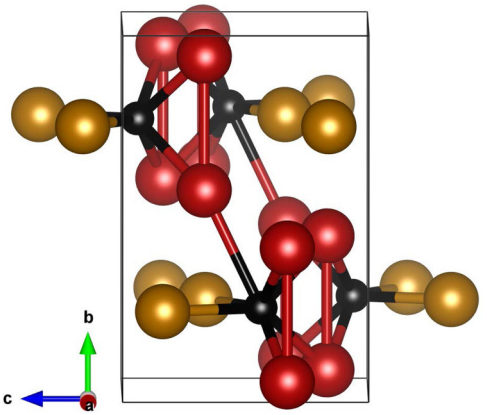

FIG. 1. Structure of cementite. Carbon atoms are black, Fe_I atoms (4*c* sites) are gold, and Fe_{II} atoms (8*d* sites) are red. Bonds with lengths below 2.5 Å are illustrated including first-nearest-neighbor Fe-C bonds comprising the trigonal prisms. The shortest Fe-Fe interatomic distance is shown (red) along with an Fe-C bond that bridges the layers of stacked trigonal prisms along the *b* axis (red/black). Figure was rendered using VESTA package [6].

was prepared by placing 95% isotopically enriched ^{57}Fe powder and graphite powder inside a MgO crucible. The crucible was placed inside a large volume press where it was held at 1 GPa and 1373 K for 102 h as in Walker *et al.* [28]. Pieces of the MgO crucible were visually and magnetically separated from the $^{57}Fe_3$ C crystals, which were ground into powder under acetone. The experimental lattice parameters of $^{57}Fe_3$ C at 300 K were confirmed by powder x-ray diffraction (XRD) using a laboratory Cu K-α source and Reitveld refinement, giving interplanar spacings very similar to synchrotron XRD measurements on other samples of Fe_3C generated by similar high pressure synthesis methods [29,30]. No iron impurity phases were observed in the sample. Comparisons are provided in the Supplemental Material [31].

Nuclear resonant inelastic x-ray scattering (NRIXS) measurements were performed on $^{57}Fe_3$ C at temperatures between 14 and 600 K. NRIXS is a low background technique that provides direct access to the phonon partial density of states (pDOS) of ^{57}Fe [32,33]. Measurements were performed at beamline 16ID-D of the Advanced Photon Source at Argonne National Laboratory using a radiative heating furnace [34]. For high-temperature measurements the powder sample was mounted on a thermocouple using Cotronics Cermabond 7020 aluminia-based ceramic compound. The NRIXS measurements performed below room temperature employed a He flow Be-dome cryostat, with the Fe_3C powder mounted with cryogenic vacuum grease. The temperatures were accurate to within ±20 K, where ambiguity comes from comparing the furnace thermocouple measurements to NRIXS-derived detailed balance temperature calculations following procedures described in the literature [35,36].

An avalanche photodiode was positioned at approximately 90° from the incident beam to collect incoherently reradiated photons. The incident photon energy was tuned to 14.413 KeV using a high-resolution silicon crystal monochromator to provide a narrow distribution of energies with a FWHM of 2.3 meV. The incident photon energy was scanned through a range of ±170 meV, centered on the nuclear resonant energy. The Phoenix software package was used to extract the pDOS from the collected NRIXS spectra [35]. The reduction procedure assumed identical NRIXS scattering properties for both Fe sites in cementite to obtain the Fe pDOS.

B. Computation

Density functional theory (DFT) calculations of ferromagnetic Fe_3C were performed for comparison with experimental results. The lattice parameters calculated by DFT are in reasonable agreement with previous computational studies, as reported in the Supplemental Material [31]. The vibrational spectra of Fe_3C were assessed by two separate methods: quasiharmonic (QH) scaled-volume calculations at 0 K, and constant-volume calculations at finite temperatures (CVFT). This allowed us to separate and distinguish the effects of quasiharmonic thermal expansion and the effects of phonon-phonon interactions in the CVFT calculations. These vibrational spectra were, in turn, used to calculate the elastic constants of cementite across a range of temperatures.

We used the Vienna Ab initio Simulation Package (VASP) [37–40] with a generalized gradient approximation (GGA) exchange correlation functional as parametrized by Perdew, Burke, and Ernzerhof [41] to calculate the vibrational spectra and elastic constants of cementite. For phonon calculations, we modeled cementite as a $2 \times 2 \times 3$ supercell of 192 atoms. Elastic constant calculations were derived from phonon calculations or performed directly on a 16-atom unit cell. With a $2 \times 2 \times 3$ supercell, we achieved convergence with respect to the system's total energy and vibrational spectra using a Monkhorst-Pack [42] generated k-point mesh of $3 \times 3 \times 3$ and a plane wave energy cutoff of 800 eV. All calculations used spin-polarized electrons to model the system as ferromagnetic.

An Fe_3C supercell was fully relaxed to find the theoretical equilibrium lattice parameters. To calculate vibrational spectra, we introduced a random set of displacements $\{\boldsymbol{u}_i | 1 \leqslant i \leqslant 192\}$ characteristic of temperature T to the relaxed supercell of 192 atoms. The displacements $\{\boldsymbol{u}_i\}$ were generated as a linear combination of plane waves

$$\boldsymbol{u}_i = \sum_k \frac{\epsilon_k^i c_k}{\sqrt{m_i}} \sqrt{-2 \ln \xi_1}\, e^{i 2\pi \xi_2}. \tag{1}$$

Here ϵ_k^i are the normal mode eigenvectors for the modes commensurate with the supercell, and m_i the mass of atom i. The amplitudes c_k are derived from the same normal modes, with the displacement length per mode given by Errea *et al.* [43]:

$$c_k = \sqrt{\frac{\hbar}{2\omega_k} \coth\left(\frac{\hbar\omega_k}{2k_B T}\right)}, \tag{2}$$

where ω_k are the normal mode frequencies. The numbers ξ_1 and ξ_2 are uniformly distributed random numbers between 0 and 1 to produce the standard Box-Muller transform for generating normally distributed amplitudes. This distribution approximates the inclusion of zero-point motion. As such, the model incorporates nonzero displacements at 0 K and connects seamlessly to the classical limit at high temperature.

We thereby generated sets of displacements for a random and representative selection of points from the phase space of the system, as described by a Bose-Einstein distribution. Static DFT calculations on these structures and postprocessing by the temperature dependent effective potential (TDEP) method [44–46] yielded the interatomic force constants and phonon DOS of Fe_3C, for both zero and finite temperatures.

The effects of temperature were calculated in two ways. First, we calculated vibrational spectra with the quasiharmonic approximation (QH) by accounting for temperature-induced volume changes to the system while using the 0 K potential energy surface. To do this, the ground state lattice parameters were scaled by the experimental thermal expansion [10] for temperatures between 0 K and 600 K in 50 K steps. Second, constant-volume finite-temperature (CVFT) calculations were performed using the equilibrium lattice parameters, but the temperature in Eq. (2) was increased to 200, 400, and 800 K, adjusting the amplitudes of displacements in the vibrational calculations to provide finite temperature effects at constant volume.

We calculated changes to the elastic constants with temperature for both the QH and CVFT series using a self-consistent method initialized with force constants obtained from phonon calculations (described further in the Supplemental Material [31]). Elastic constants were also calculated from stress-strain relationships as implemented in VASP for the QH series, and by use of the Christoffel equations and low-energy phonon group velocities from the phonon dispersion relations for the CVFT series.

III. RESULTS AND DISCUSSION

A. Phonons

Nuclear resonant inelastic x-ray scattering spectra were measured at 17 temperatures from 14 K through the magnetic transition at 460 K, up to the reported limit of material stability at 600 K [10]. The NRIXS spectra were reduced to provide the ^{57}Fe pDOS curves in Fig. 2. The pDOS show small but significant changes through this temperature range. The most apparent change is softening and broadening of the feature near 35 meV.

The lowest temperature ^{57}Fe pDOS is compared with the 0 K DFT calculated Fe pDOS in Fig. 3. The measurement is in excellent agreement with our DFT calculations when the experimental resolution is taken into account and the energy axis is scaled by 5.5% to align the mean energies of the experimental and calculated phonon spectra. The phonon partial DOS curves from DFT show that displacements of the Fe atoms dominate the low energy phonons, while carbon atom motions dominate the higher-energy phonon branches, consistent with the relative atomic masses of the Fe and C atoms.

The average phonon energies from the Fe pDOS are plotted in Fig. 4, and compared with their QH DFT counterparts. A third curve shows the thermal softening predicted with a QH model using a thermal Grüneisen parameter, $\overline{\gamma}_{\mathrm{th}}$, obtained from the 300 K bulk properties of Fe_3C as

$$\overline{\gamma}_{\mathrm{th}} = \frac{\alpha K_{\mathrm{T}} \nu}{C_{\mathrm{V}}} = 2.24, \tag{3}$$

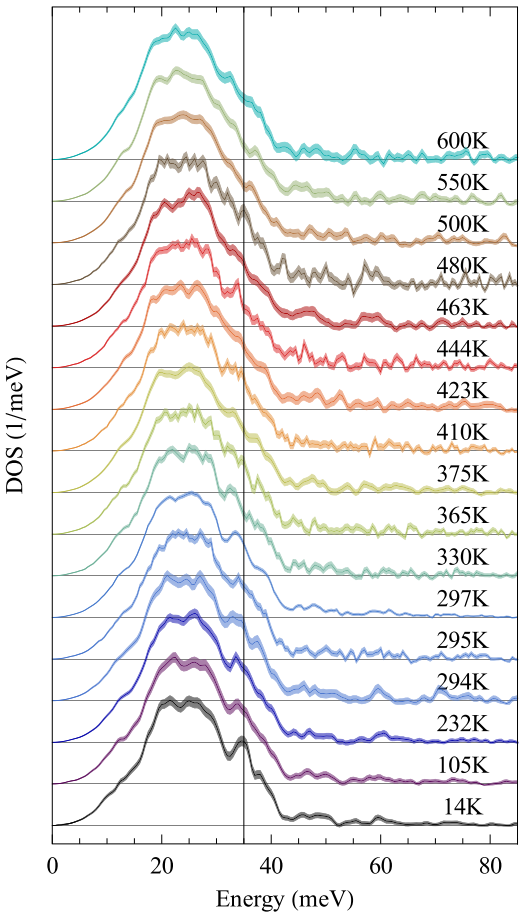

FIG. 2. Normalized ^{57}Fe pDOS extracted from NRIXS measurements at various temperatures. Statistical uncertainties are shown as shaded regions.

where K_{T} is the bulk modulus [15], α is the volume thermal expansion [10], ν is the volume per atom [10], and C_{V} is the heat capacity at constant volume calculated by integrating the DFT total phonon DOS. Both QH curves show similar trends.

The experimental average phonon energies are nearly constant (within experimental scatter) to the Curie temperature at 460 K. At higher temperatures, where cementite becomes paramagnetic, the phonon energies begin to decrease (or soften) with temperature. The QH DFT calculations predict a 0.2 meV decrease in mean phonon energy up to the magnetic transition. However, the near constant behavior of the mean phonon energy with temperature suggests there must be non-harmonic phonon behavior approximately equal and opposite to the phonon softening from thermal expansion. Above the Curie temperature the mean phonon energy decreases, following the trends of the QH models.

B. Vibrational entropy

At finite temperatures, vibrational entropy is the largest contribution to the total thermodynamic entropy of a material. The vibrational entropy can be obtained directly from measurements of the phonon DOS. In the case of phonon partial DOS measurements, a partial vibrational entropy is calculated

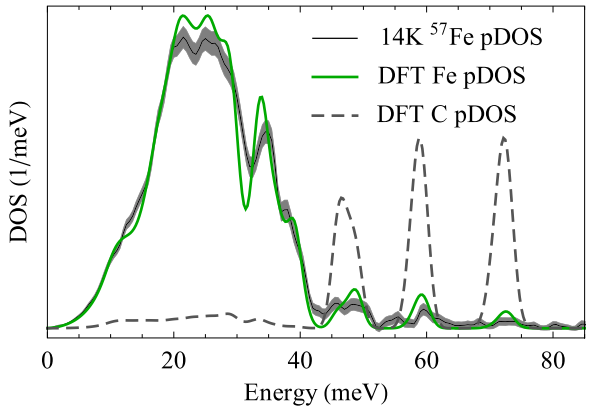

FIG. 3. ^{57}Fe pDOS from NRIXS at 14 K, compared with results from DFT. The experimental pDOS is shown in black, where the shaded region is representative of the experimental uncertainties. The DFT Fe pDOS is shown in green, along with the C pDOS (gray dashed). The energies of the DFT calculated pDOS have been scaled to match the experimental mean energies.

as

$$S_{\mathrm{vib}}^{\mathrm{Fe}}(T) = 3k_{\mathrm{B}} \int g_T^{\mathrm{Fe}}(E)\{(n+1)\ln(n+1) - n\ln(n)\}dE, \tag{4}$$

where k_{B} is the Boltzmann constant, $g_T^{\mathrm{Fe}}(E)$ is the Fe pDOS at temperature T, and n is a Planck distribution evaluated at T, for a given energy E. This expression is nonlinear in both energy and temperature, resulting in vibrational entropy values which are more sensitive to the changes in the low-energy portion of the phonon DOS, especially at low temperatures. When experimental DOS curves are available for a given temperature, this expression provides accurate entropy values that include both quasiharmonic effects and nonharmonic effects (to first order) [47].

The partial vibrational entropy, $S_{\mathrm{vib}}^{\mathrm{Fe}}(T)$, can be further divided into harmonic and nonharmonic components

$$S_{\mathrm{vib}}^{\mathrm{Fe}}(T) = S_{\mathrm{h}}^{\mathrm{Fe}}(T) + \Delta S_{\mathrm{nh}}^{\mathrm{Fe}}(T), \tag{5}$$

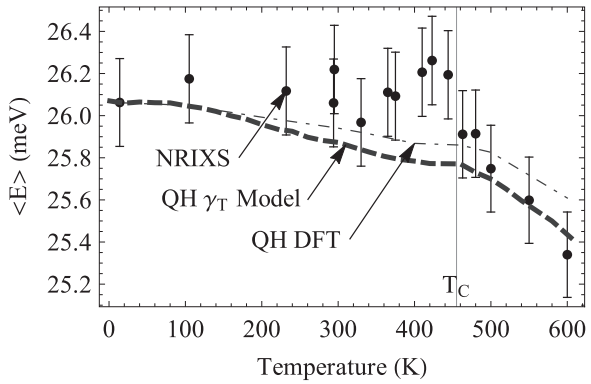

FIG. 4. Mean energy of the ^{57}Fe pDOS from NRIXS measurements with temperature (points). The thick dashed line is the mean energy calculated from a Grüneisen parameter quasiharmonic model. The thin dashed line is the Fe pDOS mean energy from quasiharmonic DFT lattice dynamics.

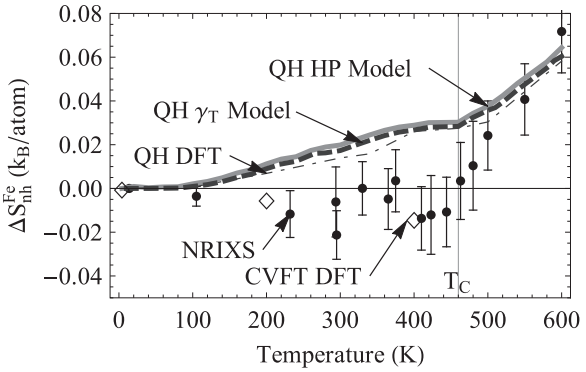

FIG. 5. Nonharmonic contributions to the Fe partial vibrational entropy, from high temperature NRIXS (points), CVFT calculations (open diamonds), and several QH models.

where $S_{\mathrm{h}}^{\mathrm{Fe}}(T)$ is harmonic vibrational entropy, which would result from a temperature invariant phonon DOS. The nonharmonic term, $\Delta S_{\mathrm{nh}}^{\mathrm{Fe}}(T)$, is defined to include the quasiharmonic contribution, $\Delta S_{\mathrm{qh}}^{\mathrm{Fe}}(T)$, the anharmonic phonon-phonon contribution, $\Delta S_{\mathrm{ah}}^{\mathrm{Fe}}(T)$, and any other contributions [48].

From the NRIXS ^{57}Fe pDOS of cementite, we obtain a partial vibrational entropy for the ^{57}Fe atoms shown in Fig. 5, along with results from quasiharmonic models. [The harmonic contribution to the vibrational entropy, $S_{\mathrm{h}}^{\mathrm{Fe}}(T)$, has been subtracted to reveal the nonharmonic behavior.] The vibrational entropy derived from QH DFT and from the Grüeneisen parameter model (QH γ_T) are compared with a quasiharmonic entropy calculated from high pressure NRIXS measurements [9] (QH HP model) as

$$\Delta S_{\mathrm{vib}}^{\mathrm{Fe}}(T) = \left.\frac{\partial S_{\mathrm{vib}}^{\mathrm{Fe}}(P)}{\partial V(P)}\right|_T \Delta V(T). \tag{6}$$

The NRIXS $\Delta S_{\mathrm{nh}}^{\mathrm{Fe}}(T)$ is lower than predicted by quasiharmonic models by 0.04 k_{B}/atom just below T_{C}, indicating a significant nonharmonic contribution that opposes the quasiharmonic contribution. The CVFT calculations do agree with the measured $S_{\mathrm{vib}}^{\mathrm{Fe}}$, but these do not include the effects of thermal expansion. Combining our CVFT results for $S_{\mathrm{vib}}^{\mathrm{Fe}}(T)$ with a correction for $\Delta S_{\mathrm{qh}}^{\mathrm{Fe}}(T)$ from QH DFT we obtain a $S_{\mathrm{vib}}^{\mathrm{Fe}}$ at 400 K that is approximately 0.025 k_{B}/atom larger than the NRIXS derived partial vibrational entropy. This suggests that other nonharmonic effects, such as magnon-phonon interactions which contribute to the high-temperature thermodynamics of Fe [34] may be responsible for a small phonon stiffening below T_{C}.

Total vibrational entropies are obtained by combining the measured $S_{\mathrm{vib}}^{\mathrm{Fe}}(T)$ with the calculated $S_{\mathrm{vib}}^{\mathrm{C}}(T)$ for each experimental temperature (provided in the Supplemental Material [31]). The total vibrational entropy values are quite close to the total vibrational entropies calculated by CVFT, provided that the calculated phonon spectra are scaled by 5.5% to align mean energies at 0 K. However, our S_{vib} values are lower than the S_{vib} calculated by previous DFT studies [21], by about 0.17 k_{B}/atom at T_{C}.

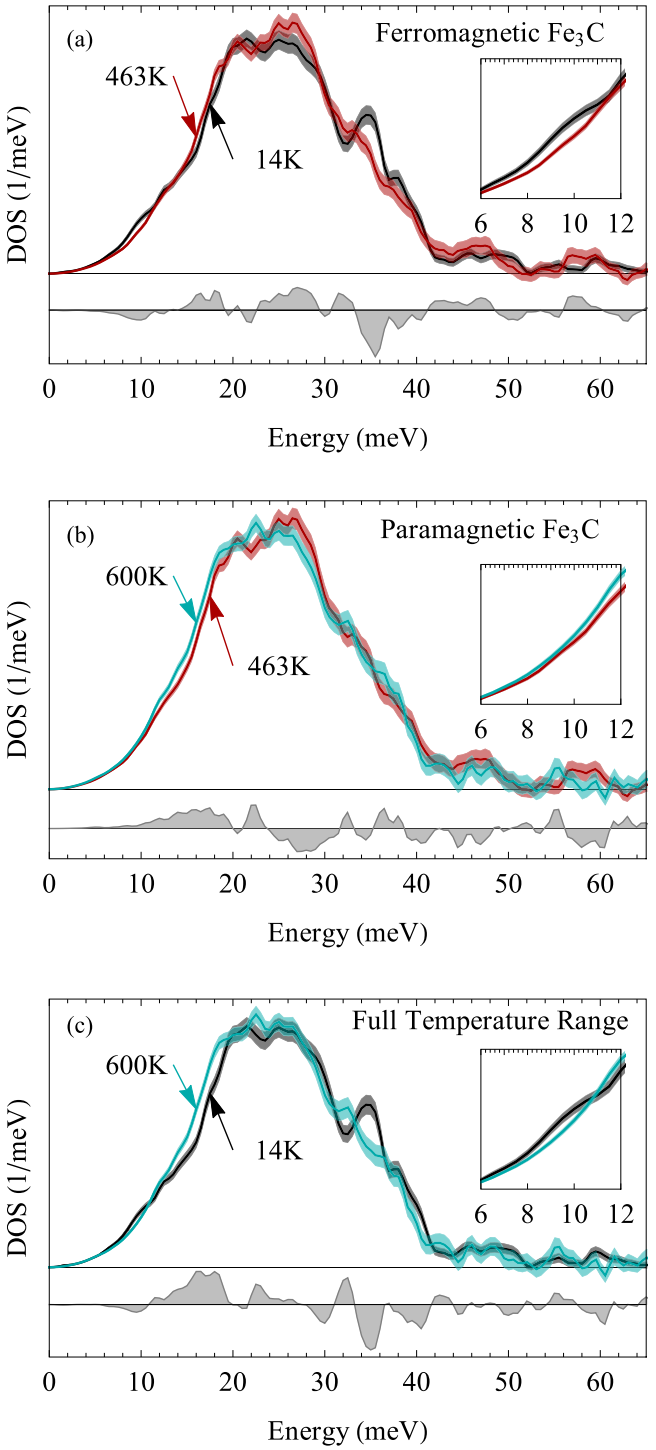

FIG. 6. ^{57}Fe pDOS compared at pairs of temperatures. Phonon difference spectra are shown beneath the phonon pDOS. The inset shows the low-energy region. Statistical uncertainties are shown as shaded regions. Panel (a) shows changes over the ferromagnetic temperatures. Panel (b) shows changes above T_C. Panel (c) compares the spectra from the highest and lowest temperatures.

C. Low-energy phonon modes

Closer examination of the low-energy phonon spectra in Fig. 6 shows that phonons below 12 meV actually stiffen (increase in energy) as the material is heated. This thermal

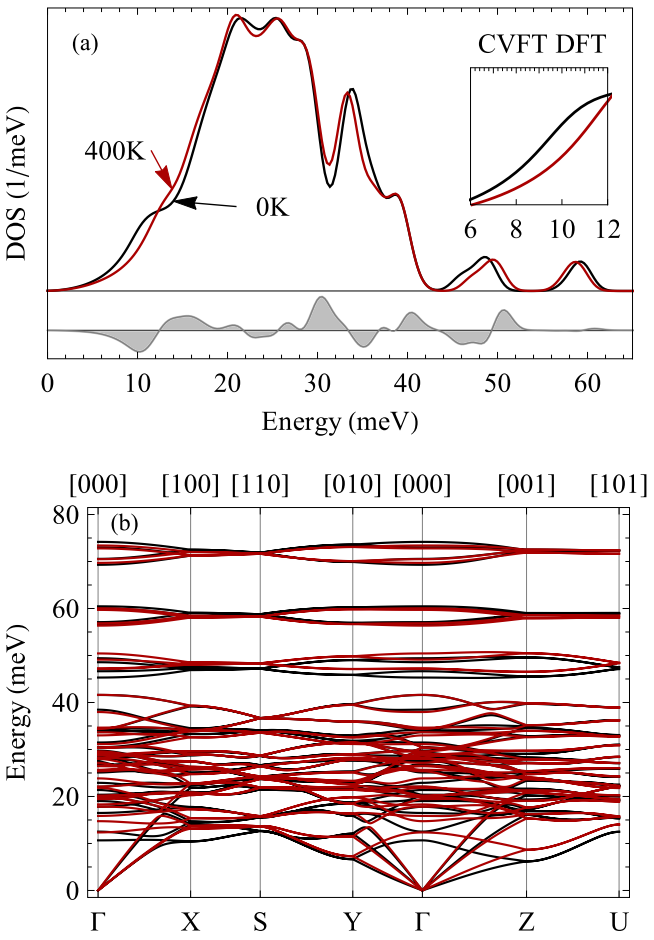

FIG. 7. Fe partial phonon DOS from CVFT calculations, convolved with an experimental resolution function, are shown in panel (a). The difference spectra are beneath, and the inset shows the changes at low energies. Panel (b) shows the corresponding phonon dispersions along high symmetry directions at 0 K (black) and 400 K (red).

stiffening is the opposite of what is expected in a material that has a net volume expansion with temperature. This anomalous stiffening of the low-energy Fe-dominated phonon modes persists up to T_C, at which point the low-energy phonons soften with temperature.

This anomalous low-energy phonon stiffening was not reproduced by quasiharmonic calculations. The QH DFT phonon dispersions soften monotonically with temperature, so the anomalous low-energy phonon stiffening in the NRIXS pDOS cannot be attributed to (anisotropic) thermal expansion. The CVFT calculations captured the anomalous thermal stiffening of low-energy modes, as shown in Fig. 7 for 0 K and 400 K. The phonon dispersions calculated using DFT at 0 K are consistent with dispersions from previous computational studies of cementite [22]. These dispersions show that the 6–12 meV shoulder in the Fe pDOS includes the van Hove singularities from the low-energy acoustic modes, and also the lowest energy optical modes near the Γ point. At elevated temperatures, these modes move to higher energies as shown in Fig. 7, resulting in a significant reduction of the low-energy shoulder in the Fe pDOS. These CVFT phonon dispersions are

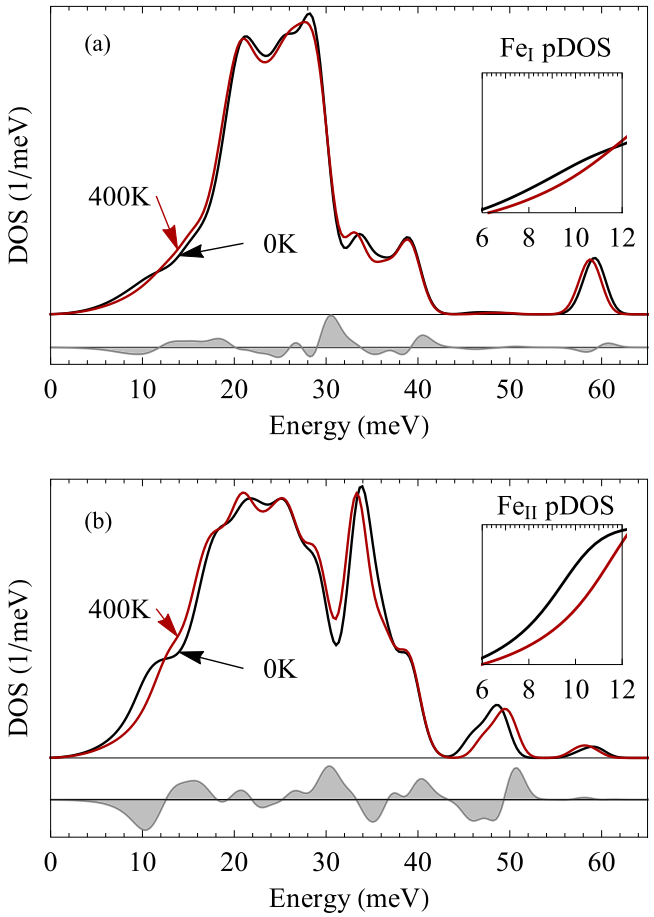

FIG. 8. Fe pDOS from CVFT calculations, convolved with an experimental resolution function, and projected onto the two distinct iron sites. Difference spectra are beneath. The inset shows the low-energy region. Panel (a) shows the Fe_I sites (four atoms/unit cell). Panel (b) shows the Fe_{II} sites (eight atoms/unit cell).

consistent with ultrasonic measurements below 300 K, which show different thermal behaviors of longitudinal and shear sound waves [27], relating to the longitudinal and transverse acoustic branches, respectively.

The transverse acoustic phonons have their lowest energies along the Γ-Z direction, and this branch stiffens noticeably with temperature, even at low q. The low-energy transverse acoustic phonon stiffening is particularly large at the X and Z points, where the lowest energy transverse acoustic phonons stiffen by 26% and 40%, respectively. Both these branches have significant polarizations along the [010] directions. In contrast, the transverse branches from Γ to Y, which do not stiffen significantly with temperature, are polarized perpendicular to the [010] direction. Several other k points along the high symmetry directions were examined, and the thermal stiffening of these modes was correlated with significant phonon polarization along the [010] direction. The two lowest-energy optical modes also show large thermal stiffening near the Γ point, with a 16% phonon energy increase for the lowest point, and a 18% energy increase for the highest point.

The calculated Fe pDOS can be subdivided for the unique Fe sites in the orthorhombic cementite structure (Fig. 8). The Fe_{II} pDOS contains much greater intensity in the low-energy phonon shoulder that exhibits the anomalous thermal stiffening. The Fe_I sites participate in these phonon modes to a lesser degree, and exhibit less thermal stiffening. Additionally, the Fe_{II} pDOS contains the prominent feature at 35 meV, which softens with temperature, although not to the same extent as the experimental NRIXS pDOS.

The Fe_{II} sites have the closest Fe-Fe bond distance in the cementite structure, which is aligned along the b axis [7]. The DFT calculations found that the shortest Fe_{II}-Fe_{II} bond has a longitudinal force constant that is noticeably larger than all other Fe-Fe second-nearest-neighbor bonds, with a magnitude comparable to the first-nearest-neighbor Fe-C interactions. The anomalous thermal stiffening of the modes below 12 meV can be reproduced by incorporating the CVFT thermal trends of the Fe_{II}-Fe_{II} and Fe_{II}-C atomic force constants into phonon calculations, with the remaining force constants held at 0 K values. Additionally, the anomalous stiffening of the phonon DOS can be largely recreated by incorporating only the thermal trends of the Fe_{II}-Fe_{II} and Fe_{II}-C forces along the b axis. This confirms that the Fe_{II} sublattice plays a crucial role in the anomalous thermal behavior of cementite below T_C. The distinct Fe sites of Fe_3C have quite different roles in the thermal phonon behavior of the material. The sites also exhibit differing electron densities of states, which are examined in the Supplemental Material [31].

D. Elastic constants

The elastic constants of cementite are reported to be highly anisotropic at 0 K, but no computational studies have reported the effects of temperature on its elastic moduli [22–24]. Elastic moduli measured at 300 K do not exhibit the extreme shear anisotropy reported from 0 K DFT calculations [25,26]. Our measurements of the Fe pDOS indicate that the acoustic modes stiffen significantly with temperature below the magnetic transition, suggesting significant temperature-driven changes to the elastic constants.

As explained in the Supplemental Material [31], thermal trends for the nine single-crystal elastic constants for orthorhombic cementite were computed using a self-consistent method that relied on calculated interatomic force constants. Six of the nine single crystal elastic constants were also calculated directly from low-energy phonon group velocities with the Christoffel equations [22]. Table I shows the calculated single crystal elastic constants of cementite alongside values

TABLE I. Single crystal elastic moduli at 0 K from self-consistent calculations, the Christoffel equations, and stress strain calculations in this study (*) compared with values reported in the literature.

Source	C_{11}	C_{22}	C_{33}	C_{12}	C_{23}	C_{13}	C_{44}	C_{55}	C_{66}
Self-consistent*	315	321	299	136	175	131	24	142	138
Christoffel*	319	321	298	...	...	...	26	140	139
Stress-strain*	383	344	300	162	162	156	28	134	135
Christoffel [22]	384	325	283	...	...	...	26	134	125
Stress-strain [22]	395	347	325	158	163	169	18	134	135
Energy [24]	385	341	316	157	162	167	13	131	131

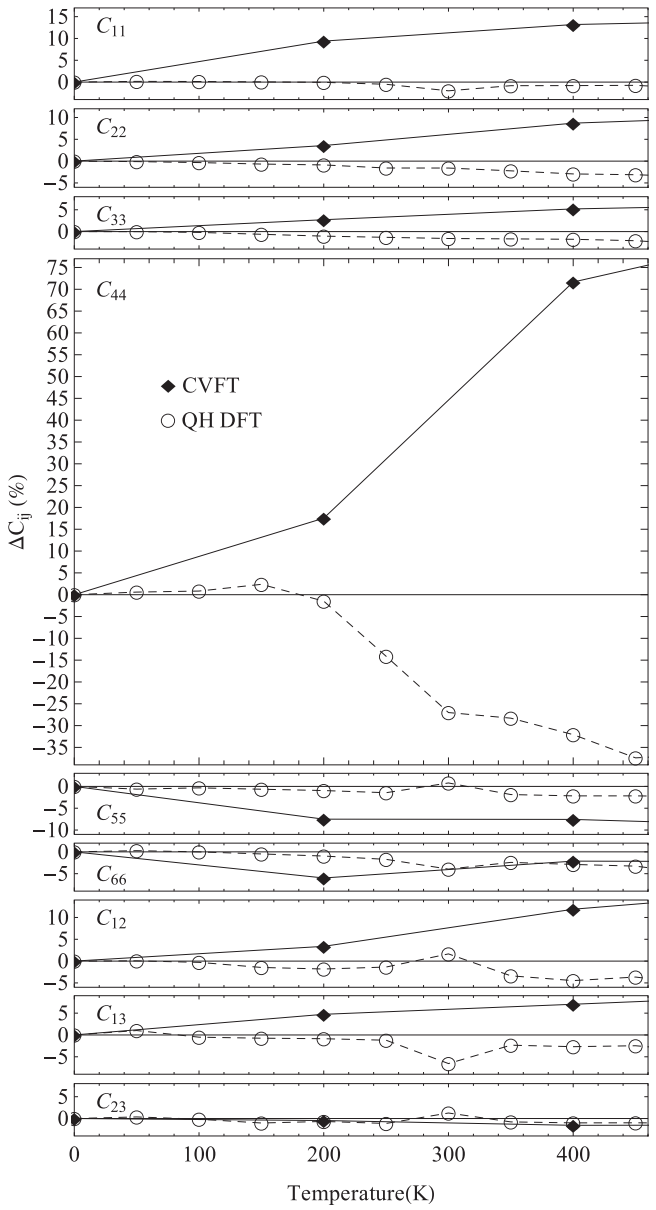

FIG. 9. Thermal trends of elastic moduli obtained using the self-consistent method with the QH and CVFT calculations.

reported in the literature. Our calculated elastic moduli at 0 K compare well with these prior results, including a C_{44} elastic constant that is quite low. However, the C_{44} elastic constant is related to the acoustic phonon branch along the Γ-Z direction, which exhibits significant anomalous thermal stiffening. In Fig. 9, we show temperature-dependent relative changes of the elastic constants of cementite according to both our QH and CVFT temperature series. The phonon-phonon interactions included in the CVFT series often oppose the trends from the QH thermal expansion, with the effects of phonon-phonon interactions clearly dominating for C_{11}, C_{22}, C_{33}, and C_{44}. For estimates of the elastic constants at temperatures above 0 K, the effects of the thermal expansion in the QH and the effects of phonon-phonon interactions in the CVFT can be added. The results are reported in Table II. In some cases the changes to the elastic constants are very significant; C_{44}, for example, increases by 38% between 0 K and 400 K. The results in Table II do not include possible effects of magnon-phonon interactions, but these are probably largest near T_C.

TABLE II. Comparison of single crystal elastic moduli (GPa) at 0 K and 400 K calculated by combining both the effects of the QH and CVFT calculations.

Temperature	C_{11}	C_{22}	C_{33}	C_{12}	C_{23}	C_{13}	C_{44}	C_{55}	C_{66}
0 K	315	321	299	136	175	131	24	142	138
400 K	354	340	309	146	171	137	33	129	131
Δ (GPa)	39	19	10	10	−4	6	7	−11	−7
%	12	6	3	7	−2	5	38	−9	−5

TABLE III. Zener ratios at 0 K and 400 K derived from single crystal elastic moduli in Table II.

Temperature	A_1	A_2	A_3
0 K	0.35	1.62	1.51
400 K	0.43	1.32	1.30

The three Zener ratios A_1, A_2, and A_3, are metrics of the elastic anisotropy. They are defined as

$$A_1 = \frac{4C_{44}}{C_{22} + C_{33} - 2C_{23}},$$
$$A_2 = \frac{4C_{55}}{C_{11} + C_{33} - 2C_{13}}, \quad (7)$$
$$A_3 = \frac{4C_{66}}{C_{11} + C_{22} - 2C_{12}}.$$

The ratios equal one in an isotropic crystal, but Table III shows that they are far from one. The ratio A_1 is exceptionally low due to the anomalously low C_{44} value of cementite, consistently reported to be near 20 GPa by computational DFT studies [22,24]. The 0 K and 400 K elastic constant values calculated by the self-consistent method were used to obtain the Zener ratios of cementite at 0 K and 400 K. By 400 K, all three Zener ratios have advanced appreciably towards one, indicating that cementite becomes significantly less anisotropic at moderate temperatures.

IV. CONCLUSIONS

Nuclear resonant inelastic x-ray scattering measurements were performed on $^{57}Fe_3C$, cementite, from 14 K to 600 K. Systematic changes in the ^{57}Fe pDOS were found, including a decrease in energy (softening) and broadening of a feature near 35 meV, and an anomalous increase in energy (stiffening) of acoustic phonons below 12 meV. The average phonon energies were approximately constant to the Curie temperature T_C, but then decreased with temperature.

The effects of temperature on the pDOS were interpreted as effects on phonon frequencies from (1) thermal expansion, calculated by density functional theory using lattice dynamics methods in the quasiharmonic approximation (QH), and (2) anharmonic phonon-phonon interactions, calculated by

constant volume finite temperature (CVFT) methods. The CVFT method accounted well for the thermal trends of the ^{57}Fe pDOS, whereas the QH approximation overestimated the thermal phonon softening. Nevertheless, we expect the presence of both the effects of volume (obtained from QH) and of pure thermal anharmonicity (obtained from CVFT), so we suggest that magnon-phonon interactions contribute a phonon stiffening at the higher temperatures of the ferromagnetic phase. The total vibrational entropy of cementite was obtained for the range of temperatures examined by combining the measured $S_{\mathrm{vib}}^{\mathrm{Fe}}(T)$ with a calculated $S_{\mathrm{vib}}^{\mathrm{C}}(T)$.

The anomalous thermal stiffening of the phonons below 12 meV was predicted well by the CVFT method, which showed thermal stiffening of long-wavelength phonon branches with polarizations along [010]. The anomalous stiffening occurs primarily in the pDOS of the $\mathrm{Fe_{II}}$ sites. This thermal stiffening originates primarily with changes in the force constant tensors describing the $\mathrm{Fe_{II}}$-$\mathrm{Fe_{II}}$ and the $\mathrm{Fe_{II}}$-C interactions.

A self-consistent method was developed to extract all nine single-crystal elastic constants from the calculated phonon behavior. This permitted the computational assessment of the elastic behavior at finite temperatures. The C_{44} elastic constant was confirmed to be quite low at 0 K, but C_{44} increased rapidly with temperature in relation to the thermal stiffening of the [100] transverse acoustic phonon mode with [010] polarization. These thermal changes of C_{44} and other elastic constants reduce the elastic anisotropy of cementite at higher temperatures in the ferromagnetic phase.

ACKNOWLEDGMENTS

The experimental equipment used in this work benefited from design discussions with Curtis Kenney-Benson and Eric Rod. This work was supported by the Department of Energy through the Carnegie-DOE Alliance Center, funded by the Department of Energy through the Stewardship Sciences Academic Alliance Program. J.E.H. was supported by the Department of Energy Office of Science Graduate Fellowship Program (DOE SCGF), made possible in part by the American Recovery and Reinvestment Act of 2009, administered by ORISE-ORAU under Contract No. DE-AC05-06OR23100. J.L. thanks Dave Walker for assistance with synthesizing the Fe_3C sample and acknowledges support from the Deep Carbon Observatory through the Sloan Foundation, NSF Grant No. AST1344133 and NSF Grant No. EAR1219891. The calculations performed herein were made possible by resources of the National Energy Research Scientific Computing Center, a DOE Office of Science User Facility supported by the Office of Science of the U.S. Department of Energy under Contract No. DE-AC02-05CH11231. Portions of this work were performed at HPCAT (Sector 16), Advanced Photon Source (APS), Argonne National Laboratory. HPCAT operations are supported by DOE-NNSA under Grant No. DE-NA0001974 and DOE-BES under Grant No. DE-FG02-99ER45775, with partial instrumentation funding by NSF. The Advanced Photon Source is a U.S. Department of Energy (DOE) Office of Science User Facility operated for the DOE Office of Science by Argonne National Laboratory under Contract No. DE-AC02-06CH11357.

[1] C. M. Fang, M. H. F. Sluiter, M. A. van Huis, C. K. Ande, and H. W. Zandbergen, Phys. Rev. Lett. **105**, 055503 (2010).
[2] J. W. Morris, Science **320**, 1022 (2008).
[3] B. J. Wood, Earth Planet. Sci. Lett. **117**, 593 (1993).
[4] M. Ron and Z. Mathalone, Phys. Rev. B **4**, 774 (1971).
[5] J. Li, H. K. Mao, Y. Fei, E. Gregoryanz, M. Eremets, and C. S. Zha, Phys. Chem. Miner. **29**, 166 (2002).
[6] K. Momma and F. Izumi, J. Appl. Crystallogr. **44**, 1272 (2011).
[7] E. J. Fasiska and G. A. Jeffrey, Acta Crystallogr. **19**, 463 (1965).
[8] D. Walker, J. Li, B. Kalkan, and S. M. Clark, American Mineralogist **100**, 2610 (2015).
[9] L. Gao, B. Chen, J. Wang, E. E. Alp, J. Zhao, M. Lerche, W. Sturhahn, H. P. Scott, F. Huang, Y. Ding, S. V. Sinogeikin, C. C. Lundstrom, J. D. Bass, and J. Li, Geophys. Res. Lett. **35**, L17306 (2008).
[10] I. G. Wood, L. Vocadlo, K. S. Knight, D. P. Dobson, W. G. Marshall, G. D. Price, and J. Brodholt, J. Appl. Crystallogr. **37**, 82 (2004).
[11] E. Duman, M. Acet, T. Hülser, E. F. Wassermann, B. Rellinghaus, J. P. Itié, and P. Munsch, J. Appl. Phys. **96**, 5668 (2004).
[12] E. Duman, M. Acet, E. F. Wassermann, J. P. Itié, F. Baudelet, O. Mathon, and S. Pascarelli, Phys. Rev. Lett. **94**, 075502 (2005).
[13] S. Khmelevskyi, A. V. Ruban, and P. Mohn, J. Phys.: Condens. Matter **17**, 7345 (2005).
[14] C. Prescher, L. Dubrovinsky, C. McCammon, K. Glazyrin, Y. Nakajima, A. Kantor, M. Merlini, and M. Hanfland, Phys. Rev. B **85**, 140402 (2012).
[15] J.-F. Lin, V. V. Struzhkin, H.-K. Mao, R. J. Hemley, P. Chow, M. Y. Hu, and J. Li, Phys. Rev. B **70**, 212405 (2004).
[16] M. Umemoto, Z. G. Liu, H. Takaoka, M. Sawakami, K. Tsuchiya, and K. Masuyama, Metallurgical and Materials Transactions A **32**, 2127 (2001).
[17] X. L. Dong, Z. D. Zhang, Q. F. Xiao, X. G. Zhao, Y. C. Chuang, S. R. Jin, W. M. Sun, Z. J. Li, Z. X. Zheng, and H. Yang, J. Mater. Sci. **33**, 1915 (1998).
[18] T. Miki and K. Ishii, ISIJ Int. **54**, 29 (2014).
[19] K. O. E. Henriksson and K. Nordlund, Phys. Rev. B **79**, 144107 (2009).
[20] B. Hallstedt, D. Djurovic, J. von Appen, R. Dronskowski, A. Dick, F. Körmann, T. Hickel, and J. Neugebauer, Calphad **34**, 129 (2010).
[21] A. Dick, F. Körmann, T. Hickel, and J. Neugebauer, Phys. Rev. B **84**, 125101 (2011).
[22] C. Jiang, S. G. Srinivasan, A. Caro, and S. A. Maloy, J. Appl. Phys. **103**, 043502 (2008).
[23] C. Jiang and S. G. Srinivasan, Nature (London) **496**, 339 (2013).
[24] M. Nikolussi, S. L. Shang, T. Gressmann, A. Leineweber, E. J. Mittemeijer, Y. Wang, and Z. K. Liu, Scr. Mater. **59**, 814 (2008).
[25] J. Alkorta and J. G. Sevillano, J. Mater. Res. **27**, 45 (2012).

[26] B.-W. Koo, Y. J. Chang, S. P. Hong, C. S. Kang, S. W. Jeong, W.-J. Nam, I.-J. Park, Y.-K. Lee, K. H. Oh, and Y.-W. Kim, Scr. Mater. **82**, 25 (2014).
[27] S. P. Dodd, G. A. Saunders, M. Cankurtaran, B. James, and M. Acet, Phys. Status Solidi A **198**, 272 (2003).
[28] D. Walker, R. Dasgupta, J. Li, and A. Buono, Contrib Miner. Petrol. **166**, 935 (2013).
[29] L. Gao, B. Chen, J. Zhao, E. E. Alp, W. Sturhahn, and J. Li, Earth Planet. Sci. Lett. **309**, 213 (2011).
[30] A. C. Larson and R. B. Von Dreele, General Structure Analysis System (GSAS), Los Alamos National Laboratory Report LAUR 86-748 (2000).
[31] See Supplemental Material at http://link.aps.org/supplemental/10.1103/PhysRevB.95.024308 for additional information on experimental and computational methods and results.
[32] A. Chumakov and W. Sturhahn, Hyperfine Interact. **123-124**, 781 (1999).
[33] W. Sturhahn and V. Kohn, Hyperfine Interact. **123-124**, 367 (1999).
[34] L. Mauger, M. S. Lucas, J. A. Muñoz, S. J. Tracy, M. Kresch, Y. Xiao, P. Chow, and B. Fultz, Phys. Rev. B **90**, 064303 (2014).
[35] W. Sturhahn, Hyperfine Interact. **125**, 149 (2000).
[36] W. Sturhahn and J. M. Jackson, Special Papers-Geol. Soc. Am. **421**, 157 (2007).
[37] G. Kresse and J. Hafner, Phys. Rev. B **48**, 13115 (1993).
[38] G. Kresse and J. Furthmüller, Comput. Mater. Sci. **6**, 15 (1996).
[39] G. Kresse and J. Furthmüller, Phys. Rev. B **54**, 11169 (1996).
[40] G. Kresse and D. Joubert, Phys. Rev. B **59**, 1758 (1999).
[41] J. P. Perdew, K. Burke, and M. Ernzerhof, Phys. Rev. Lett. **77**, 3865 (1996).
[42] H. J. Monkhorst and J. D. Pack, Phys. Rev. B **13**, 5188 (1976).
[43] I. Errea, M. Calandra, and F. Mauri, Phys. Rev. B **89**, 064302 (2014).
[44] O. Hellman, I. A. Abrikosov, and S. I. Simak, Phys. Rev. B **84**, 180301 (2011).
[45] O. Hellman, P. Steneteg, I. A. Abrikosov, and S. I. Simak, Phys. Rev. B **87**, 104111 (2013).
[46] O. Hellman and I. A. Abrikosov, Phys. Rev. B **88**, 144301 (2013).
[47] D. C. Wallace, *Thermodynamics of Crystals* (Dover Publications, New York, 1998).
[48] B. Fultz, Prog. Mater. Sci. **55**, 247 (2010).